Inorganic Chemistry
ARTICLE
pubs.acs.org/IC

Fe-Site Substitution Effect on the Structural and Magnetic Properties in $SrFeO_2$

Liis Seinberg,[†,‡,§] Takafumi Yamamoto,[†,‡] Cédric Tassel,[†,‡] Yoji Kobayashi,[†] Naoaki Hayashi,[∥]
Atsushi Kitada,[†,‡] Yuji Sumida,[†,‡] Takashi Watanabe,[‡] Masakazu Nishi,[⊥] Kenji Ohoyama,[#]
Kazuyoshi Yoshimura,[‡] Mikio Takano,[@] Werner Paulus,[§] and Hiroshi Kageyama*[,†,‡,@]

[†]Department of Energy and Hydrocarbon Chemistry, Graduate School of Engineering, Kyoto University, Kyoto 615-8510, Japan
[‡]Department of Chemistry, Graduate School of Science, Kyoto University, Kyoto 606-8502, Japan
[§]University of Rennes 1, Sciences Chimiques de Rennes, UMR 6226 Bât. 10B, Campus de Beaulieu, F-35042 Rennes, France
[∥]Graduate School of Human and Environmental Studies, Kyoto University, Kyoto 606-8501, Japan
[⊥]Institute for Solid State Physics, University of Tokyo, 5-1-5 Kashiwanoha, Kashiwa, Chiba, 277-8581, Japan
[#]Institute for Materials Research, Tohoku University, 2-1-1 Katahira, Aoba-ku, Sendai 980-8577, Japan
[@]Institute for Integrated Cell-Material Sciences, Kyoto University, Kyoto 606-8501, Japan

Supporting Information

ABSTRACT: We investigated the Fe-site substitution effect on the structural and magnetic properties of the infinite layer iron oxide $Sr(Fe_{1-x}M_x)O_2$ (M = Co, Mn) using synchrotron X-ray diffraction, neutron diffraction, and ^{57}Fe Mössbauer spectroscopy. Both systems have a similar solubility limit of $x \approx 0.3$, retaining the ideal infinite layer structure with a space group of *P*4/*mmm*. For the Fe−Co system, both in-plane and out-of-plane axes decrease linearly and only slightly with *x*, reflecting the ionic radius difference between Fe^{2+} and Co^{2+}. For the Fe−Mn system the lattice evolution also follows Vegard's law but is anisotropic: the in-plane axis increases, while the out-of-plane decreases prominently. The magnetic properties are little influenced by Co substitution. On the contrary, Mn substitution drastically destabilizes the *G*-type magnetic order, featured by a significant reduction and a large distribution of the hyperfine field in the Mössbauer spectra, which suggests the presence of magnetic frustration induced presumably by a ferromagnetic out-of-plane Mn−Fe interaction.

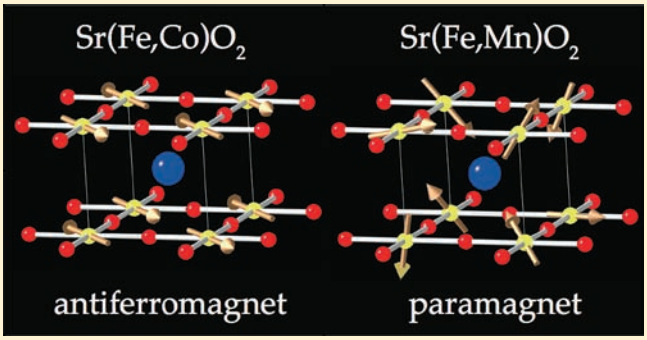

1. INTRODUCTION

$SrCu^{2+}O_2$ can adopt an infinite layer (IL) structure (Figure 1), the simplest structure among nondoped parent structures for high-temperature superconducting cupper oxides.[1] At ambient pressure, solid solutions of this compound are not readily formed, existing only as the solid solution $(Sr_{1-x}Ca_x)CuO_2$ in a narrow composition region ($0.86 < x < 0.91$). High-pressure synthesis can expand the solubility range to $(Sr_{1-x}Ca_x)CuO_2$ ($0 \leq x < 0.9$)[2] and $(Sr_{1-x}Ba_x)CuO_2$ ($0 < x < 0.33$).[3] It becomes a superconductor when moderate carriers are injected into the CuO_2 layer under high pressure, as first reported by $(Sr_{1-x}Nd_x)CuO_2$.[4]

A topochemical low-temperature reducing reaction of a perovskite $LaNi^{3+}O_3$ with metal hydrides yielded an isostructural compound $LaNi^{+}O_2$ in the form of either powder[5] or thin film.[6] $LaNi^{+}O_2$ film could also be fabricated by metal organic decomposition.[7] Formation of $LaNiO_2$ or the NiO_4 square planar coordination is understandable from the viewpoint of solid state chemistry because a monovalent nickel is in the d^9 electronic configurations and is a Jahn−Teller active ion as in the case of divalent copper. The lack of superconductivity in this nickelate makes an interesting contrast with the isoelectronic cuprate.

Recently, another isostructural system $SrFe^{2+}O_2$ was prepared by metal hydride topotactic reduction using a perovskite $SrFeO_3$ (or a brownmillerite $SrFeO_{2.5}$) in the form of powder[8] and thin film.[9] $SrFeO_2$ exhibits magnetic order with a *G*-type spin structure as found in $SrCuO_2$, and its Néel temperature T_N is as high as 473 K. The upmost feature in this iron oxide is the FeO_4 square planar coordination geometry in spite of a Jahn−Teller inactive nature of d^6 electronic configurations. Previous studies have demonstrated that $SrFeO_2$ bears a substantial stability against the substitution for Sr, up to 100% of calcium,[10] and up to 30% of barium.[11] However, the *A*-site substitution has little influence on the magnetic order, as evidenced by only a small

Received: December 9, 2010
Published: March 31, 2011

dx.doi.org/10.1021/ic102467u | *Inorg. Chem.* 2011, 50, 3988–3995

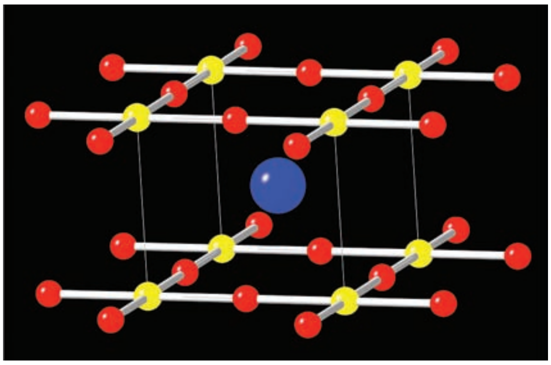

Figure 1. Crystal structure of the infinite layer (IL) structure ABO_2 ($SrFeO_2$), where blue, yellow, and red balls represent, respectively, *A*-site (Sr), *B*-site (Fe), and oxygen atoms. The unit cell is shown by the solid lines.

change of the hyperfine field *HF* in the Mössbauer spectra at room temperature (RT) (HF = 40.2 T for $SrFeO_2$ and $(Sr_{0.2}Ca_{0.8})FeO_2$[12] and HF = 39.1 T for $(Sr_{0.7}Ba_{0.3})FeO_2$[11]).

In this paper, we performed the *B*-site (Fe) substitution by Co and Mn. The main motivations are two-fold. (I) Structural stability: first-principles calculations based on density functional theory have revealed that $SrFeO_2$ is indeed a thermodynamically stable phase with strong in-plane and out-of-plane exchange interactions.[13,14] Therefore, although the IL structure of $SrMnO_2$ and $SrCoO_2$ has not yet been reported and $Co^{2+}O_4$ and $Mn^{2+}O_4$ square planar coordination is very rarely obtained,[15−17] we expect that such a coordination can exist as a solid solution $Sr(Fe_{1-x}M_x)O_2$ (M = Co, Mn) to a certain extent. (II) Controlling physical properties: $SrFeO_2$ shares structural features with the recently discovered iron pnictide superconductors in that the iron ions are coordinated 4-fold and form a two-dimensional square lattice. It has been shown in the iron pnictides that electron doping by Fe-to-Co substitution leads to superconductivity.[18,19] In addition, knowing that application of pressure to $SrFeO_2$ induces three simultaneous transitions, i.e., a spin state transition from a high-spin ($S = 2$) to an intermediate-spin ($S = 1$) state, an insulator-to-metal transition, and an antiferromagnetic-to-ferromagnetic transition,[20] the Mn^{2+} (d^5) and Co^{2+} (d^7) substitution at the Fe^{2+} (d^6) site in $SrFeO_2$ may correspond, respectively, to hole and electron doping, giving rise to potential novel magnetic and transport properties.

2. EXPERIMENTAL SECTION

Precursors $Sr(Fe_{1-x}Mn_x)O_3$ and $Sr(Fe_{1-x}Co_x)O_3$ (x = 0.1, 0.2, 0.3, 0.4) were prepared using high-temperature solid state reactions from $SrCO_3$ (99.99%), Fe_2O_3 (99.99%), Mn_3O_4 (99.99%), and Co_3O_4 (99.99%) purchased from Rare Metallic Ltd. The appropriate mixture of the starting regents was ground thoroughly, pelletized, and preheated at 1000 °C for 24 h. After being reground and pelletized, the pellets were heated again at 1200 °C for 24 h. The reduction of $Sr(Fe_{1-x}M_x)O_3$ was carried out using two molar excess of CaH_2. The mixture was ground and pelletized in an Ar-filled glovebox and was sealed in an evacuated Pyrex tube (volume 15 cm^3) with a residual pressure of less than 1.3×10^{-8} MPa. The samples were reacted at 250 °C for 24 h. After the hydride reduction process, residual CaH_2 and CaO byproduct were removed from the products by washing them with 0.1 M of NH_4Cl in dried methanol solution. The obtained compounds are all black and insulating.

The X-ray diffraction data were collected on Mac Science MXP18 diffractometer equipped with a graphite monochromator and a Cu K_α source (1.5406 Å). The powder synchrotron X-ray diffraction experiments on $Sr(Fe_{1-x}Mn_x)O_2$ (x = 0.1, 0.2, 0.3) were performed at RT on the large Debye−Scherrer camera installed at the source of BL02B2 in the Synchrotron Radiation Research Institute SPring-8 in Japan. We used an imaging plate as a detector. The incident beam from a bending magnet was monochromatized to 0.7749 Å. The sample powder was sealed in a Pyrex capillary with an inner diameter of 0.1 mm. The synchrotron data were collected on a 2θ range from 0° to 75° with an interval step of 0.01°. Unfortunately, we could not obtain the synchrotron X-ray diffraction data on the Co-substituted samples because of the limited beam time and the instability of the substituted samples, which are air sensitive. We also observed that they tend to decompose with time even in the argon-filled glovebox.

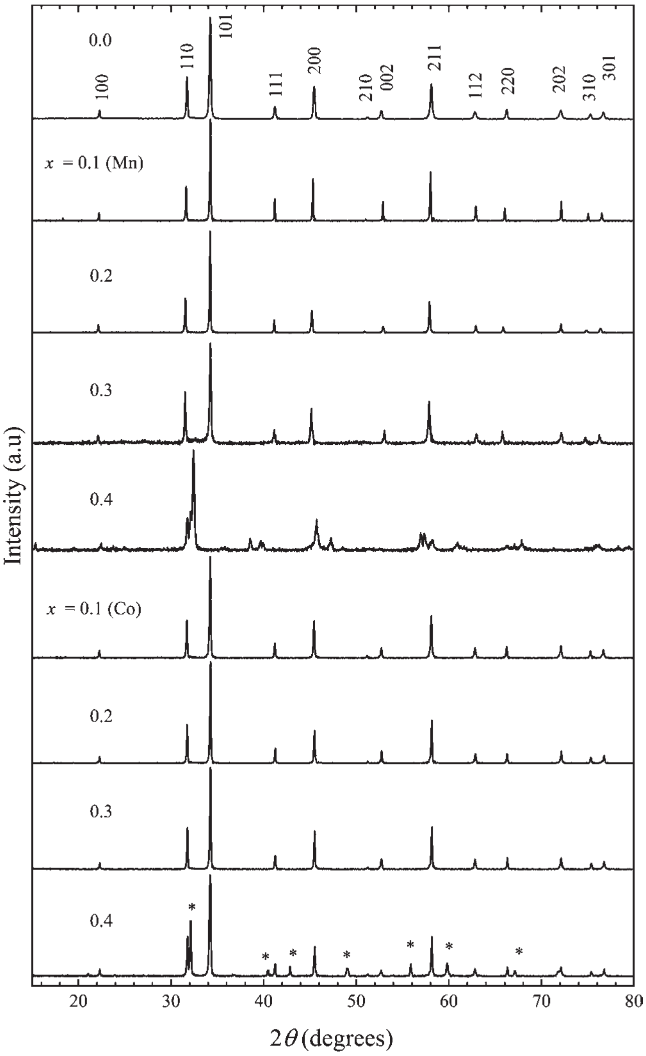

Figure 2. RT powder XRD patterns of the products after the low-temperature reduction of $Sr(Fe_{1-x}M_x)O_2$ (M = Co, Mn; x = 0,[8] 0.1, 0.2, 0.3, 0.4). Impurity peaks in x = 0.4 (Co) are indicated by an asterisk (*). The perovskite-based framework is completely decomposed for x = 0.4 (Mn).

Powder neutron diffraction experiments on $Sr(Fe_{1-x}M_x)O_3$ (M = Co, Mn; x = 0.1, 0.2, 0.3) were carried out at RT on the Kinken powder diffractometer for high-efficiency and high-resolution measurements with multicounters, HERMES, of the Institute for Materials Research (IMR), Tohoku University, installed at the guide hall of the JRR-3 reactor in the Japan Atomic Energy Agency (JAEA), Tokai.[21] The incident neutron with a wavelength of 1.8204 Å was

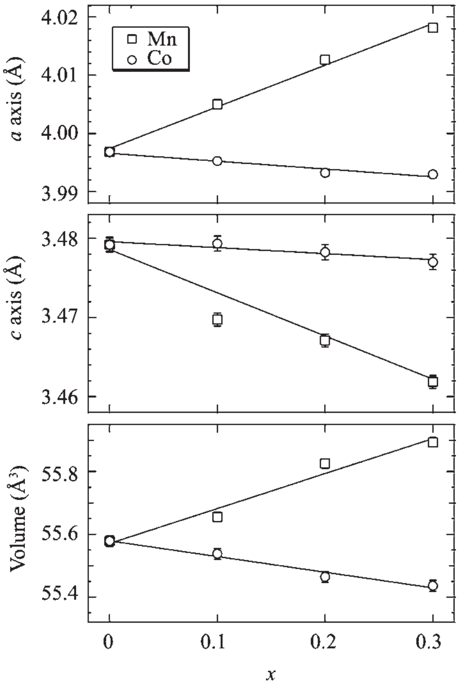

Figure 3. Unit cell parameters of $Sr(Fe_{1-x}M_x)O_2$ (M = Co (circles), Mn (squares); x = 0,[8] 0.1, 0.2, 0.3) at RT.

monochromatized by the 331 reflection of a Ge crystal. The 12′-blank-sample-18′ collimation was employed. A polycrystalline sample of about 4 g mass was placed into a vanadium cylinder. For the sake of comparison, the end phase $SrFeO_2$ was also measured. Data was collected with the step-scan procedure using 150 neutron detectors in a 2θ range from 3° to 153° with a step width of 0.1°. Due to the air sensitivity of the sample, the neutron diffraction pattern for $SrFe_{0.7}Co_{0.3}O_2$ has a higher background (~1000 counts) than the others (~250 counts). In addition, the background intensity becomes higher at lower angles, which is possibly due to the presence of moisture. This background causes relatively high errors of the thermal parameters in the Rietveld refinement.

The obtained synchrotron XRD and neutron data were analyzed by the Rietveld method using JANA2006[22] and the RIETAN-FP program.[23] The agreement indices used were R-weighted pattern, $R_{wp} = [\Sigma w_i(y_{io} - y_{ic})^2/\Sigma w_i(y_{io})^2]^{1/2}$, R pattern, $R_p = \Sigma|y_{io} - y_{ic}|/\Sigma(y_{io})$, and goodness of fit (GOF), $\chi^2 = [R_{wp}/R_{exp}]^2$, where $R_{exp} = [(N - P)/\Sigma w_i y_{io}{}^2]^{1/2}$, y_{io} and y_{ic} are the observed and calculated intensities, w_i is the weighting factor, N is the total number of y_{io} data when the background is refined, and P is the number of adjusted parameters.

^{57}Fe Mössbauer spectroscopy measurements were carried out at RT. The data were collected in transmission geometry using an ^{57}Fe γ-ray source in combination with a constant-acceleration spectrometer. The source velocity was calibrated using α-Fe. The obtained spectra were fitted with the Lorentzian function programmed by Prof. N. Hosoito.

■ RESULTS AND DISCUSSION

The purity of the $Sr(Fe_{1-x}M_x)O_{3-y}$ (x = 0.1, 0.2, 0.3 and 0.4) precursors was confirmed by laboratory X-ray diffraction. For each solid solution, all diffraction peaks were indexed in a (pseudo) cubic unit cell, consistent with the reported data[24,25] (see Figure S1, Supporting Information). No impurity phase was detected within the accuracy of our experiment. As shown in Figure 2, the laboratory X-ray diffraction patterns of both Mn and Co systems (x = 0.1, 0.2 and 0.3) after CaH_2 reduction were readily indexed in a tetragonal unit cell. Lattice parameters calculated by the least-squares fitting of selected peaks are plotted as a function of x in Figure 3, together with the data for $SrFeO_2$ (x = 0).[8] For each solid solution system, the linear dependence of the lattice parameters, i.e., Vegard's law, can be seen in this concentration range, suggesting successful synthesis of the solid solution. However, the x = 0.4 specimen contained, together with the IL phase for M = Co, a large amount of impurity phases that could not be indexed. Thus, the solubility limit for both solid solutions should be $x \approx 0.3$.

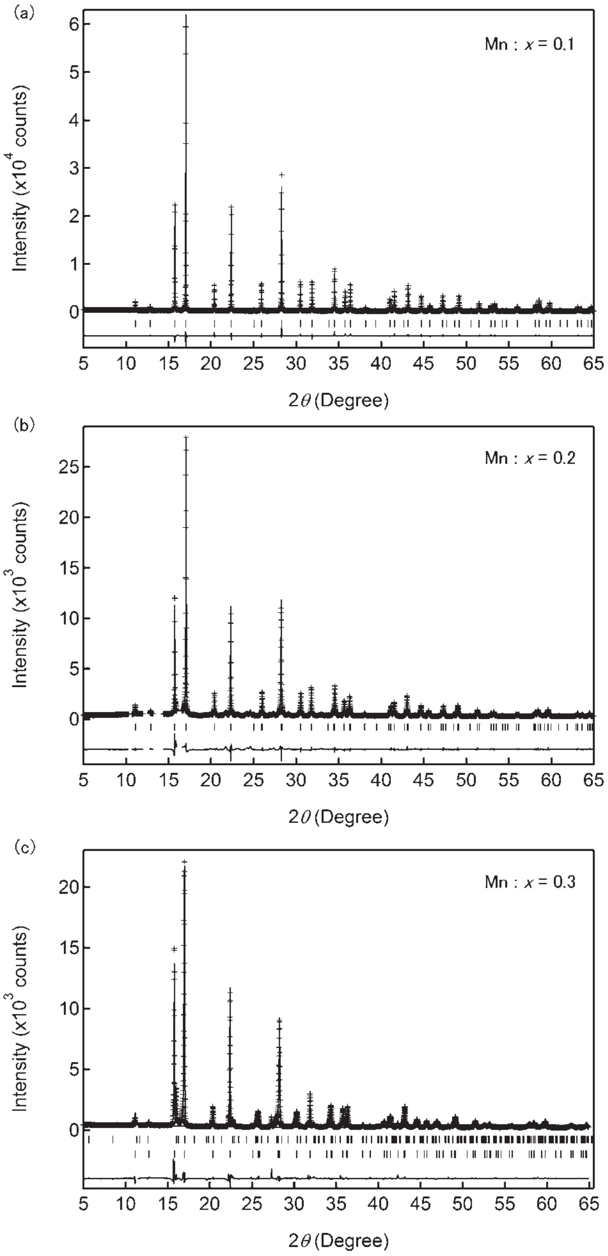

Figure 4. Observed (crosses), calculated (lines), and difference plots from the structural refinement of the powder synchrotron XRD data for $Sr(Fe_{1-x}Mn_x)O_2$ (x = 0.1, 0.2, 0.3). The ticks represent the positions of the calculated Bragg reflections. The lower ticks for x = 0.3 (Mn) represent the positions of the calculated Bragg reflections of the brownmillerite-type $SrFeO_{2.5}$ structure.

A marked difference exists between the two solid solutions (see Figure 3): the concentration dependence of the volume is opposite in its sign, namely, negative and positive for M = Co and Mn, respectively, and the ratio $|dV/dx|$ is greater for M = Mn than for Co. The behavior in the Co case can be understood in terms of the difference in the ionic radius between Fe^{2+} (0.64 Å) and Co^{2+} (0.58 Å) in a high-spin state.[26] However, interpretation of the behavior in the Mn case is not at all straightforward given the similar ionic radii of Mn^{2+} (0.66 Å) and Fe^{2+}.[26] Furthermore, the composition dependence of lattice parameters is anisotropic in M = Mn: the in-plane length increases, while the out-of-plane length decreases. At this stage, we do not have any explicit explanation of the anisotropic lattice evolution, but these anomalous behaviors tell us the necessity to consider a model beyond the simple hard-sphere model.

Table 1. Synchrotron XRD Rietveld Refinement for $Sr(Fe_{1-x}Mn_x)O_2$ (x = 0.1, 0.2, 0.3)

	x in $Sr(Fe_{1-x}Mn_x)O_2$		
	0.1	0.2	0.3
a (Å)	3.9947(3)	3.9990(4)	4.0083(8)
c (Å)	3.4878(2)	3.4611(2)	3.4490(2)
B in Sr (Å^2)	0.71(3)	0.42(1)	0.45(3)
B in M (Å^2)	0.11(3)	0.32(1)	0.47(4)
B in O (Å^2)	0.96(7)	0.46(3)	0.90(9)
R_{wp} (%)	9.51	6.61	9.52
R_p (%)	5.84	4.78	6.27
χ^2	4.32	1.83	4.72

[a] All refinements were performed using the ideal IL structure, $P4/mmm$ space group with Sr on 1d (1/2,1/2,1/2), $(Fe_{1-x}Mn_x)$ on 1a (0, 0, 0), and O on 2f (1/2, 0, 0).

The high-resolution synchrotron X-ray diffraction patterns for $Sr(Fe_{1-x}Mn_x)O_2$ (x = 0.1−0.3) can also be indexed in a tetragonal unit cell. A brownmillerite-type ($SrFeO_{2.5}$) phase and an unknown impurity were detected as a minor impurity for x = 0.3 and 0.2, respectively, but additional peaks originating from superstructure peaks as observed in $CaFeO_2$ could not be detected.[27] The peak widths of the target phase do not differ from the nonsubstituted $SrFeO_2$ sample, demonstrating that the crystallinity of the B-site-substituted samples is as good as that of $SrFeO_2$. Rietveld structural refinement of $Sr(Fe_{1-x}Mn_x)O_2$ (x = 0.1−0.3) was performed using the ideal IL structure with the space group $P4/mmm$ as a starting model. For x = 0.3, the brownmillerite-type phase was introduced as the secondary phase. The Fe and Mn atoms were distributed randomly, and thermal parameters of all atoms are allowed to vary. The refinement converged rapidly, yielding reasonable thermal parameters. Figure 4 represents the typical results of the refinement, and Table 1 summarizes the details of refined parameters.

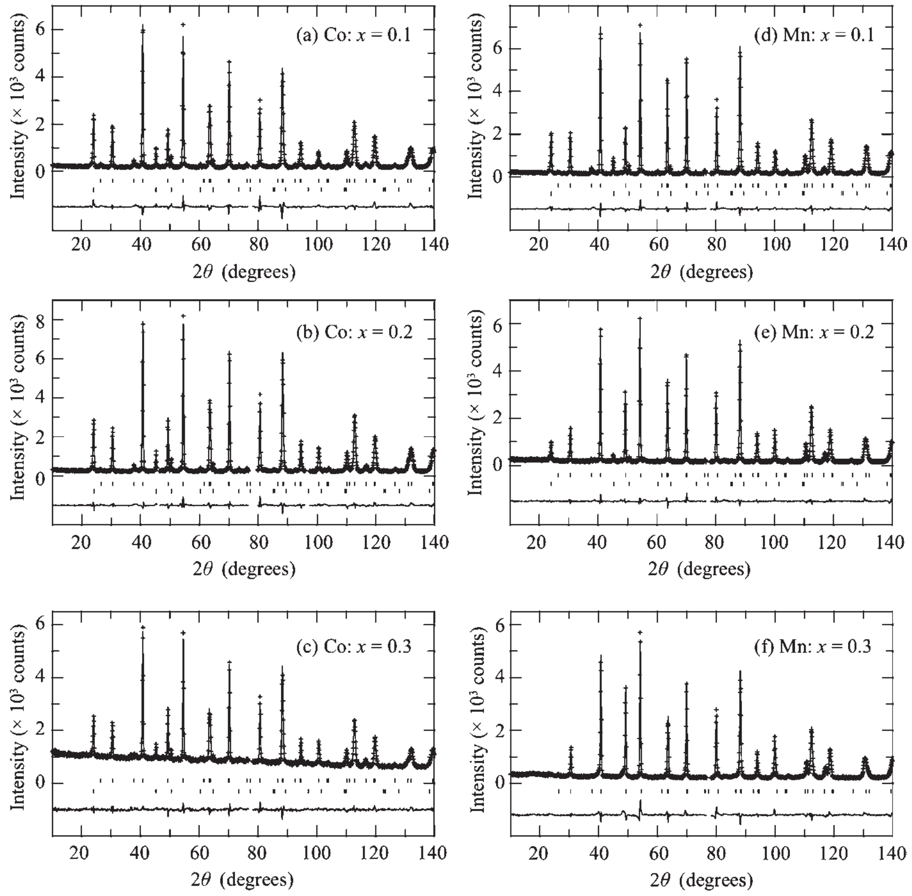

Figure 5. Observed (crosses), calculated (lines), and difference plots from the structural refinement of the powder neutron data for (left) $Sr(Fe_{1-x}Co_x)O_2$ (x = 0.1, 0.2, 0.3) and (right) $Sr(Fe_{1-x}Mn_x)O_2$ (x = 0.1, 0.2, 0.3). The upper and lower ticks represent the positions of the calculated chemical and magnetic Bragg reflections (except x = 0.3, Mn).

Table 2. Neutron Rietveld Refinement for $Sr(Fe_{1-x}M_x)O_2$ ($M = Co, Mn$; $x = 0.1, 0.2, 0.3$)

	x in $Sr(Fe_{1-x}Co_x)O_2$			x in $Sr(Fe_{1-x}Mn_x)O_2$		
	0.1	0.2	0.3	0.1	0.2	0.3
a (Å)	3.9797(3)	3.9794(2)	3.9764(3)	3.9928(2)	4.0005(2)	4.0055(1)
c (Å)	3.4653(2)	3.4643(1)	3.4648(2)	3.4609(1)	3.4548(1)	3.4553(1)
B in Sr (Å^2)	0.45(6)	0.42(5)	0.3(6)	0.41(5)	0.50(5)	0.42(7)
B in M (Å^2)	0.4(3)	0.4(2)	0.4(7)	0.38(4)	0.40(4)	0.21(6)
B in O (Å^2)	0.75(5)	0.78(4)	0.9(10)	0.74(4)	0.82(4)	0.91(5)
moment (μ_B)	3.1	3.0	2.7	3.0	1.9	0
R_{wp} (%)	8.24	7.09	4.03	8.29	7.68	9.11
R_p (%)	6.45	5.56	3.20	6.38	5.82	7.01
χ^2	2.69	2.64	1.66	2.67	2.13	3.37

[a] All refinements were performed using the ideal IL structure, $P4/mmm$ space group with Sr on 1d (1/2,1/2,1/2), ($Fe_{1-x}M_x$) on 1a (0, 0, 0), and O on 2f (1/2, 0, 0).

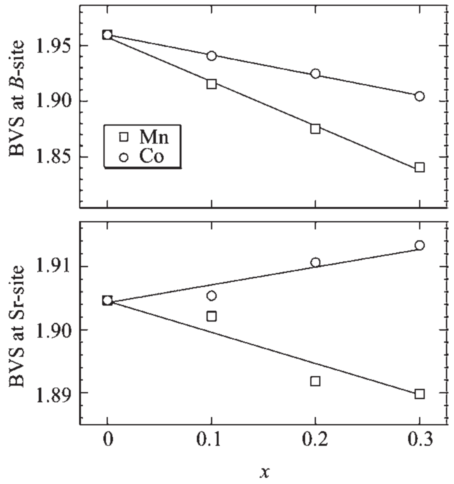

Figure 6. B-site BVS (upper) and Sr BVS (lower) as a function of x. We assumed $r_0(B) = (1 - x)r_0(\mathrm{Fe}) + xr_0(M)$, where $r_0(\mathrm{Fe}) = 1.734$ Å, $r_0(\mathrm{Co}) = 1.692$ Å, and $r_0(\mathrm{Mn}) = 1.790$ Å.[24] Squares and circles denote, respectively, the Mn system and Co system. Tabulated values corresponding to high-spin Fe, Co, and Mn were employed.[24] The lines are the guides to the eyes.

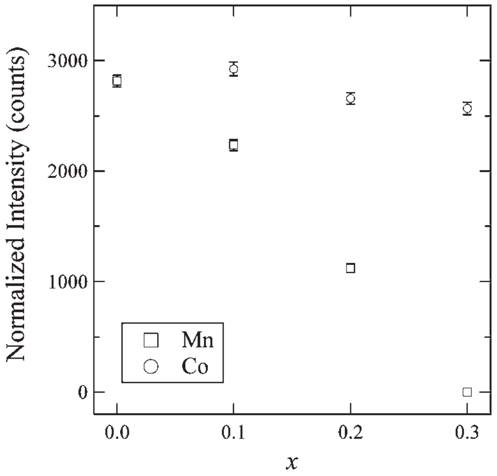

Figure 7. x dependence of the (1/2 1/2 1/2) magnetic reflection $Sr(Fe_{1-x}M_x)O_2$ (M = Co (circles) and Mn (squares)) at RT.

Neutron diffraction revealed the nuclear and magnetic structures. As shown in Figure 5, additional peaks to those originating from the nuclear structure as described above were indexed (except for $x = 0.3$; M = Mn) using an enlarged tetragonal unit cell related to the synchrotron X-ray cell by $\sqrt{2}a \times \sqrt{2}a \times 2c$. They could be naturally ascribed to the G-type antiferromagnetic order which was already found in the nonsubstituted $SrFeO_2$.[8] The neutron Rietveld refinement for all profiles was also converged immediately when the IL structure was assumed. When the site occupancy factor for the oxygen atom is allowed to vary, it scarcely changed, indicating a stoichiometric oxygen content of 2. We thus confirm that $Sr(Fe_{1-x}M_x)O_2$ ($x \leq 0.3$) crystallizes in the ideal IL structure. The results of Rietveld structural refinement of the neutron diffraction data are represented in Figure 5, and full details of the refined parameters are provided in Table 2.

The bond valence sum (BVS) calculations[28] were performed for Sr and the B site, and the results are shown in Figure 6. The Sr BVS increases (decreases) only slightly with Mn (Co) substitution. The BVS at the B site for M = Mn decreases rapidly with x, deviating from the formal valence of +2. The BVS at the B site for M = Co also decreases with x, which appears to contradict the reduced in-plane lattice but is in fact originating from the difference in the empirically determined parameter r_0 between Co ($r_0(\mathrm{Co}) = 1.692$ Å) and Fe ($r_0(\mathrm{Fe}) = 1.734$ Å).[28] The difference of r_0 between Fe and Mn is -0.056 Å ($r_0(\mathrm{Mn}) = 1.790$ Å), which is greater in magnitude than that between Fe and Co (0.042 Å). This can essentially explain the a-axis expansion for the Mn solid solution. Here, the orbital occupancy might contribute to the considerable contraction of the c axis for Mn. First-principles calculations of $SrFeO_2$ performed by several independent groups demonstrated that the sixth down-spin electron occupies the z^2 orbital, providing the 3d electronic configurations of $(d_{z2})^2(d_{xz},d_{yz})^2(d_{xy})^1(d_{x2-y2})^1$.[13,14] Such electronic configurations result from electrostatic and hybridization effects. This double occupation of the z^2 orbital would be partially removed by replacing Fe^{2+} with Mn^{2+} with one less d electron, i.e. $(d_{z2})^1(d_{xz},d_{yz})^2(d_{xy})^1(d_{x2-y2})^1$. We propose that the depopulation of the d_{z2} orbital can reduce the repulsion between the out-of-plane orbitals and allow contraction of the c axis.

Let us move onto the discussion of the magnetic properties. Figure 7 shows the concentration dependence of the (1/2 1/2 1/2) magnetic reflection. Here the intensity was normalized by the (1 1 0) nuclear reflection. One can see for M = Co that the intensity of the magnetic reflection decreases only slightly with x. In contrast, in the case of Mn the magnetic reflection decreases drastically and disappears at $x = 0.3$. This result indicates a significant reduction of T_N with x and that $x = 0.3$ (Mn) is in a paramagnetic state at RT. The magnetic moment of the iron in $SrFeO_2$ at RT is 3.1 μ_B ($x = 0$) and aligns perpendicular to the c axis.[8] We assumed the same alignment of the magnetic moment and estimated the averaged magnetic moment of the B site as 3.1 μ_B ($x = 0.1$), 3.0 μ_B ($x = 0.2$), and 2.7 μ_B ($x = 0.3$) for Co and 3.0 μ_B ($x = 0.1$) and 1.9 μ_B ($x = 0.2$) for Mn. Note that it is difficult to judge whether Co^{2+} and Mn^{2+} ions take a high- or low-spin state solely from the RT neutron data. However, the nearly invariant magnetic moment observed for the Co solid solution implies a high-spin state ($S = 3/2$).

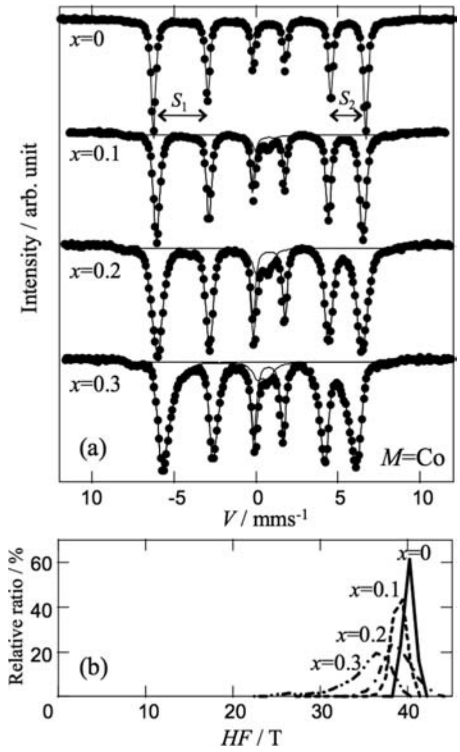

Figure 8. (a) ^{57}Fe Mössbauer spectra of $Sr(Fe_{1-x}Co_x)O_2$ ($x = 0$,[8] 0.1, 0.2, 0.3) at RT. Circles are the experimental data. The data were fitted by a sextet originating from the IL phase and a doublet originating from the Fe^{3+}-containing amorphous impurity. The corresponding subspectrum was given by the broken line, and the total fit was given by the solid line. (b) Distribution of the hyperfine field *HF*. The relative area is plotted with an interval of 1 T.

Table 3. Mössbauer Parameters for $Sr(Fe_{1-x}M_x)O_2$ (M = Co, Mn; x = 0.1, 0.2, 0.3) at Room Temperature

M	x	*IS* (mms^{-1})	*HF* (T)	*QS* (mms^{-1})	area (%)
Co	0 [b]	0.498	40.2	1.16 [c]	100
	0.1	0.494	39.0 [a]	1.10 [c]	100
	0.2	0.499	38.7 [a]	1.14 [c]	100
	0.3	0.484	35.2 [a]	1.12 [c]	100
Mn	0.1	0.500	33.0 [a]	1.12 [c]	100
	0.2	0.561	26.1 [a]	1.32 [c]	77
		0.500	0	1.22	23
	0.3	0.467	0	1.29 [a]	100

[a] Averaged value. [b] From ref 8. [c] $S_1 - S_2$.

All Mössbauer spectra for M = Co at RT (Figure 8a) have a well developed sextet indicative of long-range magnetic order. The separation of the sextet decreases very slowly and proportionally with x, indicating a slight reduction in T_N, which is in accordance with the neutron diffraction results. Note that each spectrum contains a small amount of doublet component, which can be attributed to a Fe^{3+}-containing amorphous impurity formed during the hydride reduction, as also reported in $(Sr,Ca)FeO_2$[10] and $(Sr,Ba)FeO_2$.[11] Thus, in the following we will focus on the sextet part, intrinsic to the infinite layer phase. The sextet spectra were fitted using *HF*, quadrupole splitting *QS* (which should be derived from $S_1 - S_2$ in Figure 8a), and isomer shift *IS* as adjustable parameters. This initial fitting revealed that *IS* and *QS* are nearly unchanged with x. However, the spectrum peaks of the substituted samples, especially the two outer lines, show a broadening compared to the rest of spectra, meaning a small distribution of *HF* caused by the random substitution of foreign Co ions on the iron site. Accordingly, the fitting of each spectrum was performed allowing a distribution of *HF* to vary while maintaining *QS* and *IS*. To be more explicit, each magnetic spectrum was analyzed as a superposition of sextets having an intensity ratio of 3:2:1:1:2:3 with the full width at half-maximum of 0.27 mm/s but with a different *HF*. The Mössbauer parameters were given in Table 3, and the obtained distribution of *HF* is plotted in Figure 8b. It can be seen that the average value of *HF* for $Sr(Fe_{0.7}Co_{0.3})O_2$ is slightly decreased to 35.2 T from 40.2 T in $SrFeO_2$. Since $CaFeO_2$ with T_N = 420 K has *HF* = 34.7 T at RT,[12,27] it is likely that the T_N of $Sr(Fe_{0.7}Co_{0.3})O_2$ has a higher T_N than $CaFeO_2$, namely, the reduction of T_N with respect to $SrFeO_2$ would be no more than 50 K. The *IS* and *QS* values do not show considerable change with x due to preservation of the local environment of iron against substitution.

On the other hand, the Fe-to-Mn substitution influences the Mössbauer spectrum to a greater extent (Figure 9a). For example, the *HF* of $Sr(Fe_{0.9}Mn_{0.1})O$ at RT is around 33 T, which is much smaller than that of $Sr(Fe_{0.9}Co_{0.1})O_2$ and is rather close to the average value of 35.2 T in $Sr(Fe_{0.7}Co_{0.3})O_2$. Moreover, $Sr(Fe_{0.9}Mn_{0.1})O_2$ has a more prominent distribution of *HF* than $Sr(Fe_{0.7}Co_{0.3})O_2$. The x = 0.2 (Mn) spectrum is comprised of two subspectra, a sharp doublet and a much broadened sextet. The x = 0.3 spectrum consists only of a doublet, consistent with the neutron diffraction data showing a paramagnetic state. The Mn spectra were also fitted introducing a distribution of *HF* (see Figure 9b). We would like to stress that the larger distribution of *HF* is not simply due to poor crystallinity but due to competing ferro- and antiferromagnetic interactions, because XRD and neutron diffraction for both Co and Mn systems showed equally sharp peaks. The calculated *IS* and *QS* values do not change with x, like in the Co-substituted samples, which clearly indicates that the $(Fe,Mn)O_4$ square planar coordination is preserved as shown by structural analysis.

The coexistence of a doublet and sextet in the x = 0.2 (Mn) spectrum at RT implies the presence of magnetically ordered and disordered phases. It was already argued that all samples are homogeneous in terms of the crystal structure within the resolution of the synchrotron X-ray. It should be noted that Mössbauer spectra of low-dimensional magnets have a tendency to show the coexistence of a doublet and sextet in the vicinity of a transition temperature,[29] which could be due to local concentration inhomogeneities, local strain, and so on. The present Mn solid solution has an inevitable concentration inhomogeneities. In particular, in the presence of frustration, as is the case with the Mn system, this local inhomogeneity, even if it is tiny, could have a significant influence on the magnetic properties.

From the neutron and Mössbauer experiments, we demonstrated that Mn substitution at the iron site significantly destabilizes the *G*-type magnetic order. Destabilization of the *G*-type order should arise from competing magnetic interactions that do not exist in the pure phase $SrFeO_2$. First-principles calculations on $SrFeO_2$ showed that $J_{Fe-O-Fe}$ and J_{Fe-Fe} are both antiferromagnetic (~ 3 and ~1 meV, respectively),[13,14] and recent inelastic neutron scattering experiments obtained a good quantitative agreement.[30] The Goodenough–Kanamori rule states, when M and M′ are in the high-spin d^6 and d^5 states, that the

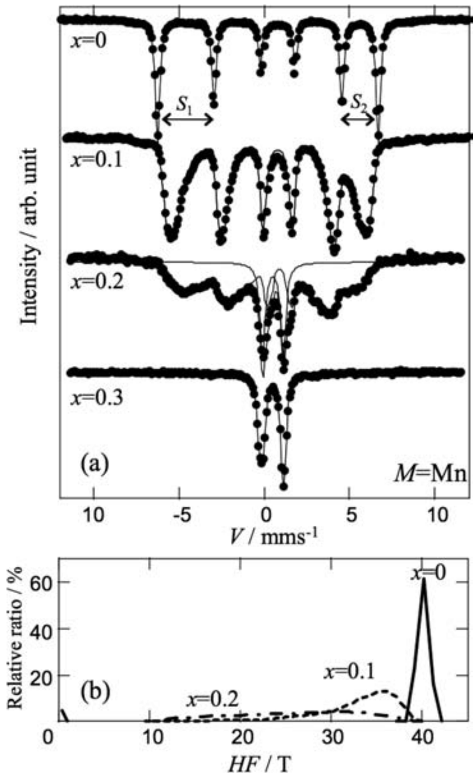

Figure 9. (a) ^{57}Fe Mössbauer spectra of $Sr(Fe_{1-x}Mn_x)O_2$ ($x = 0$,[8] 0.1, 0.2, 0.3) at RT. Circles are the experimental data. Each subspectrum was given by the broken line, and the total fit was given by the solid line. (b) Distribution of the hyperfine field *HF*.

180° M–O–M′ superexchange interaction is antiferromagnetic. Accordingly, the 180° Fe^{2+}–O–Mn^{2+} in the plane $J_{Fe-O-Mn}$, must be antiferromagnetic.

The Goodenough–Kanamori rule also states that the M–M′ direct exchange interaction (J_{Fe-Mn}) can be either antiferromagnetic or ferromagnetic depending on subtle structural differences.[31] It is thus difficult to know the sign of the direct exchange between the out-of-plane Fe^{2+} and Mn^{2+}, J_{Fe-Mn}, solely from the structural data. However, the significant destabilization of the *G*-type magnetic order strongly suggests that J_{Fe-Mn} is ferromagnetic and competes strongly with the antiferromagnetic J_{Fe-Fe}. It follows that a further substitution (if possible) would result in a phase transition to a (π, π, 0) type spin structure. Although the present study shows that the solubility limit is 30%, the solubility range may be expanded by modifying synthetic conditions (e.g., by using other metal hydrides such as LiH and NaH), which is in progress. It is also crucial to perform Mössbauer and neutron diffraction experiments on the Mn-substituted solid solution as a function of temperature, for example, a new magnetic structure might be observed in the $x = 0.2$ sample at lower temperature.

■ CONCLUSION

We showed that the *B*-site substitution in the IL structure $SrFe^{2+}O_2$ is tolerable up to 30% for both Co^{2+} and Mn^{2+}. For the Fe–Co solid solution, a linear and slow decrease of the in-plane and out-of-plane cell parameters is observed, which is explained on the basis of the ionic radii of the *B*-site cations, Fe^{2+} and Co^{2+}. Co substitution has only small effect on the magnetic properties. For the Fe–Mn solid solution, the lattice evolution is linear but quite anisotropic featured by the increase of the *a* axis and the decrease of the *c* axis. Mn substitution results in a significant reduction of the Néel temperature, indicating the presence of ferromagnetic and antiferromagnetic interactions. Although *B*-site substitution with different numbers of d electrons failed to induce a metallicity, external stimuli such as light, pressure, and magnetic fields may offer a chance to change the electromagnetic properties of the Fe–Co and Fe–Mn solid solutions. In particular, high-pressure study is interesting because the nonsubstituted $SrFeO_2$ shows the spin-state transition, the insulator-to-metal transition, and the antiferromagnetic-to-ferromagnetic transitions at 33 GPa.[20] These transitions and critical pressure could be influence by *B*-site substitution, which will be reported in the future.

■ ASSOCIATED CONTENT

Ⓢ Supporting Information. Experimental details and characterization data for the new compounds. This material is available free of charge via the Internet at http://pubs.acs.org.

■ AUTHOR INFORMATION

Corresponding Author

*E-mail: kage@scl.kyoto-u.ac.jp.

■ ACKNOWLEDGMENT

We thank N. Kawashima, R. Tamura, and Y. Motome for helpful discussions. This work was supported by Grants-in-Aid for Science Research in the Priority Areas "Novel States of Matter Induced by Frustration" (No. 19052004) and by a Grant-in-Aid for Scientific Research (A) (No. 22245009) from the Ministry of Education, Culture, Sports, Science and Technology of Japan, the Global COE program International Center Science, Kyoto University, Japan, and by the Japan Society for the Promotion of Science (JSPS) through its "Funding Program for World-Leading Innovative R&D on Science and Technology (FIRST) Program". T.Y. was supported by the Japan Society for the Promotion of Science for Young Scientists.

■ REFERENCES

(1) Siegrist, T.; Zahurak, S. M.; Murphy, D. W; Roth, R. S. *Nature* **1988**, *334*, 231–232.

(2) Ohashi, N.; Imagawa, H.; Tsurumi, T.; Fukunaga, O. *Physica C* **1997**, *278*, 71–77.

(3) Takano, M.; Takeda, Y.; Okada, H.; Miyamoto, M.; Kusaka, T. *Physica C* **1989**, *159*, 375–378.

(4) Smith, M. G.; Manthiram, A.; Zhou, J.; Goodenough, J. B.; Markert, J. T. *Nature* **1991**, *351*, 549–551.

(5) Hayward, M. A.; Green, M. A.; Rosseinsky, M. J.; Sloan, J. *J. Am. Chem. Soc.* **1999**, *121*, 8843–8854.

(6) Kawai, M.; Matsumoto, K.; Ichikawa, N.; Mizumaki, M.; Sakata, O.; Kawamura, N.; Kimura, S.; Shimakawa, Y. *Cryst. Growth Des.* **2010**, *10*, 2044–2046.

(7) Kaneko, D.; Yamagishi, K.; Tsukada, A.; Manabe, T.; Naito, M. *Physica C* **2009**, *469*, 936–939.

(8) Tsujimoto, Y.; Tassel, C.; Hayashi, N.; Watanabe, T.; Kageyama, H.; Yoshimura, K.; Takano, M.; Ceretti, M.; Ritter, C.; Paulus, W. *Nature* **2007**, *450*, 1062–1065.

(9) Inoue, S.; Kawai, M.; Shimakawa, Y.; Mizumaki, M.; Kawamura, N.; Watanabe, T.; Tsujimoto, Y.; Kageyama, H.; Yoshimura, K. *Appl. Phys. Lett.* **2008**, *92*, 161911.

(10) Tassel, C.; Watanabe, T.; Tsujimoto, Y.; Hayashi, N.; Kitada, A.; Sumida, Y.; Yamamoto, T.; Kageyama, H.; Takano, M.; Yoshimura, K. *J. Am. Chem. Soc.* **2008**, *130*, 3764–3765.

(11) Yamamoto, T.; Li, Z.; Tassel, C.; Hayashi, N.; Takano, M.; Isobe, M.; Ueda, Y.; Ohayama, K.; Yoshimura, K.; Kobayashi, Y.; Kageyama, H. *Inorg. Chem.* **2010**, *49*, 5957–5962.

(12) Unpublished work.

(13) Pruneda, J. M.; Íñiguez, J.; Canadell, E.; Kageyama, H.; Takano, M. *Phys. Rev. B* **2008**, *78*, 115101.

(14) Xiang, H. J.; Wei, S-H; Whangbo, M.-H. *Phys. Rev. Lett.* **2008**, *100*, 167207.

(15) Adkin, J. J.; Hayward, M. A. *Inorg. Chem.* **2008**, *47*, 10959–10964.

(16) Vreshch, V. D.; Yang, J.-H.; Zhang, H.; Filatov, A. S.; Dikarev, E. V. *Inorg. Chem.* **2010**, *49*, 8430–8434.

(17) Zhu, W.-J.; Hor, P. H. *J. Solid State Chem.* **1997**, *130*, 319–321.

(18) Leithe-Jasper, A.; W. Schnelle, W.; C. Geibel, C.; Rosner, H. *Phys. Rev. Lett.* **2008**, *101*, 207004.

(19) Sefat, A. S.; Huq, A.; McGuire, M. A.; Jin, R.; Sales, B. C.; Mandrus, D.; Cranswick, L. M. D.; Stephens, P. W.; Stone, K. H. *Phys. Rev. B* **2008**, *78*, 104505.

(20) Kawakami, T.; Tsujimoto, Y.; Kageyama, H.; Chen, X.-Q; Fu, C. L.; Tassel, C; Kitada, A.; Suto, S.; Hirama, K.; Sekiya, Y.; Makino, Y.; Okada, T.; Yagi, T.; Hayashi, N.; Yoshimura, K.; Nasu, S.; Podloucky, R.; Takano, M. *Nat. Chem.* **2009**, *1*, 371–376.

(21) Ohoyama, K.; Kanouchi, T; Nemoto, M; Kajitani, T.; Yamauchi, Y. *Jpn. J. Appl. Phys.* **1998**, *37*, 3319–3326.

(22) Petricek,V.; Dusek, M.; Palatinus, L. *Jana2006, The crystallographic computing system*; Institute of Physics: Praha, Czech Republic, 2006.

(23) Izumi, F.; Momma, K. *Solid State Phenom.* **2007**, *130*, 15–20.

(24) Kawasaki, S.; Takano, M.; Takeda, Y. *J. Solid State Chem.* **1996**, *121*, 174–180.

(25) Aksenova, T. V.; Gavrilova, L. Ya.; Cherepanov, V. A. *J. Solid State Chem.* **2008**, *181*, 1480–1484.

(26) Shannon, R. D. *Acta Crystallogr.* **1976**, *A32*, 751–767.

(27) Tassel, C.; Pruneda, J. M.; Hayashi, N.; Watanabe, T.; Kitada, A.; Tsujimoto, Y.; Kageyama, H.; Yoshimura, K.; Takano, M.; Nishi, M.; Ohoyama, K.; Mizumaki, M.; Kawamura, N.; Íñiguez, J.; Canadell, E. *J. Am. Chem. Soc.* **2009**, *131*, 221–229.

(28) Brown, I. D; Altermatt, D. *Acta Crystallogr.* **1985**, *B41*, 244–247.

(29) Hayashi, N.; Kageyama, H.; Tsujimoto, Y.; Watanabe, T.; Muranaka, S.; Ono, T.; Nasu, S.; Ajiro, Y.; Yoshimura, K.; Takano, M. *J. Phys. Soc. Jpn.* **2010**, *79*, 123709.

(30) Tomiyasu, K.; Kageyama, H.; Lee, C.; Whangbo, M. H.; Tsujimoto, Y.; Yoshimura, K.; Taylor, W. J.; Lobet, A.; Trouw, F.; Kakurai, K.; Yamada, K. *J. Phys. Soc. Jpn.* **2010**, *79*, 034707.

(31) Goodenough, J. B. *Magnetism and the Chemical Bond*; John Wiley & Sons: New York, 1963.